Stability analysis for *n*-periodic arrays of fluid systems

Peter J. Schmid[*]

Department of Mathematics, Imperial College London, London SW7 2AZ, United Kingdom

Miguel Fosas de Pando[†]

Department of Mechanical Engineering and Industrial Design, University of Cádiz, 11519 Puerto Real, Spain

N. Peake[‡]

Department of Applied Mathematics and Theoretical Physics, University of Cambridge,
Cambridge CB3 0WA, United Kingdom

A computational framework is proposed for the linear modal and nonmodal analysis of fluid systems consisting of a periodic array of *n* identical units. A formulation in either time or frequency domain is sought and the resulting block-circulant global system matrix is analyzed using roots-of-unity techniques, which reduce the computational effort to only one unit while still accounting for the coupling to linked components. Modal characteristics as well as nonmodal features are treated within the same framework, as are initial-value problems and direct-adjoint looping. The simple and efficient formalism is demonstrated on selected applications, ranging from a Ginzburg-Landau equation with an *n*-periodic growth function to interacting wakes to incompressible flow through a linear cascade consisting of 54 blades. The techniques showcased here are readily applicable to large-scale flow configurations consisting of *n*-periodic arrays of identical and coupled fluid components, as can be found, for example, in turbomachinery, ring flame holders, or nozzle exit corrugations. Only minor corrections to existing solvers have to be implemented to allow this present type of analysis.

I. INTRODUCTION

Fluid systems consisting of an array of identical subunits are common in many industrial configurations. Prominent among them are high-performance axial or radial turbines, compressors, and pumps where a specific number of blades are mounted on a circular hub. Other applications that fall under the same category are ring flame holders in combustion chambers, injection devices in afterburners, or the corrugated aircraft-engine nacelles intended to diminish jet-induced noise. In these configurations the geometry of each individual subunit is identical and so is the flow behavior in it (see Fig. 1 for an example and a sketch). Consequently, it seems tempting to analyze the flow through a single unit in isolation and account for the influence of neighboring components via periodic boundary conditions. While this practice has been widely applied, it is easy to demonstrate that it cannot capture a range of fluid motion (in particular, multimodal fluid instabilities) that may be important for the safe and efficient operation of an *n*-periodic fluid device. More specifically, modal solutions that are periodic over the entire *n* units, but nonperiodic over individual or multiple units, are excluded by a one-unit analysis with periodic boundary conditions.

A global analysis, i.e., treating the entire *n*-component geometry, would remedy this shortcoming, but would yield a discretized system of excessive, or even prohibitive, size. Although we will start our

---

[*]pjschmid@imperial.ac.uk
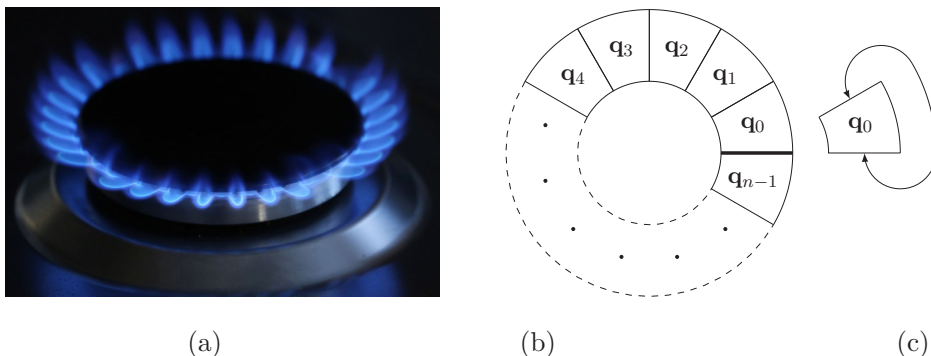
[†]miguel.fosas@uca.es

[‡]n.peake@damtp.cam.ac.uk

FIG. 1. (a) Example of an n-periodic fluid system: a gas-stove burner. (b) Sketch of an n-periodic fluid system consisting of n identical subunits described by the respective state vector $\mathbf{q}_j$, $j = 0, \ldots, n - 1$. (c) Analysis of a single unit with imposed periodic boundary conditions.

development from a formulation of the full global system, we will exploit its block-circulant structure to reduce it to a modified single-unit system, thus achieving the computational cost of isolated-unit periodic analyses while correctly modeling the full interaction with all $n - 1$ subcomponents. In addition, the breakdown into a single subunit and its subsequent linear analysis exhibits ideal scalability on a parallel computer architecture, demonstrating additional benefits for this type of analysis.

The ubiquity of fluid systems characterized by an n-periodic arrangement of identical units or by multiperiodic geometric features has spawned a great deal of analyses and simulations: Flow in wavy or grooved channels [1–4] or past arrays of roughness elements and vortex generators [5], acoustics in periodic wave-guides [6], energy extraction from a buoy array [7], and of course flow in turbomachines [8–14] and combustors [15–21] are but a few examples that fall under this category. Not surprisingly, specific analysis and simulation techniques that efficiently address this periodicity have been developed, in particular for turbomachinery applications, typically describing blade-to-blade dynamics, aeroelastic properties, and rotor-stator interactions. Among the proposed and frequently employed techniques are the harmonic-balance method [22,23], which treats time-periodic flow as a sequence of matched frequencies, the phase-lagged boundary condition method [8], which employs phase-shifted flow variables on the interface between individual subunits, and, closely related, the chorochronic boundary condition method [9,10,12,13], which generalizes the former techniques to multiple (and distinct) periodicity by an appropriate time shift. In particular, the phase-lagged and chorochronic boundary conditions are commonly used in time-periodic flow, for example, in the periodic forcing of a turbomachinery blade passage by upstream stators or rotors. In this case, the implemented phase shifts account for the time delay in the forcing that the boundaries experience. The above techniques deal with a variety of geometric configurations and flow situations that exhibit a spatial (commonly azimuthal or discrete-rotational) periodicity, time periodicity, or both.

Closest to the framework used in this article is the analysis of periodic systems using Bloch waves [24]. In a Bloch wave formalism a relation between the solution in each subunit in the form of a geometric series is presumed. The geometric factor can be interpreted as a phase shift between solutions in various units and is related to a cross-unit Bloch wave number. Substituting this ansatz into the governing equations yields a parametrized sequence of equations for the fundamental solution in a single unit [6,16]; the parameter is the Bloch wave number.

In this article we alternatively propose and use a linear-algebra approach, taking advantage of the block-circulant nature of the linearized governing equations, for spectral analysis or initial-value problems. Among the well-known properties of block-circulant matrices is the analytic nature of the symbol curve [25], which takes on a particularly compact form for nearest-neighbor couplings that are often encountered in physical and engineering applications. This symbol curve can be computed without *a priori* committing to a specific number of individual subunits. It is then

discretized along its arc length according to the number n of subunits, which subsequently yields the spectrum of the n-periodic system. The discretized symbol curve represents the mapping of roots of unity under the respective block matrices, where the indices of the roots correspond to the associated Bloch wave number. In addition to spectral (modal) properties, which mirror their equivalents in Bloch wave theory, appropriate matrix functions, as used in a nonmodal stability or receptivity analysis, can also be formulated in a very compact manner and the interaction between any two subunits can be quantified and assessed, giving a measure of perturbation propagation across subunits. The direct application of the formalism to matrix functions avoids the recasting into an eigenvalue problem, involving the adjoint operator. Finally, rather than a reformulation of the governing equations using Bloch wave theory, the proposed formalism can be straightforwardly implemented in existing simulation codes with little effort and minimal modifications.

The article is organized as follows. Starting from a full global description of an n-periodic fluid system, Sec. II will introduce practical tools to arrive at a single-unit problem and to recover the complete global dynamics from solutions of this single unit. A range of analysis tools will be treated for modal (Sec. II A) and nonmodal stability analyses (Sec. II B), impulse response, frequency response, and interunit analyses (Sec. II C) and direct-adjoint looping (Sec. II D). Implementation strategies and access details to software used in this article are given in Sec. II E. Section III gives demonstrations of the presented tools, starting with simple model equations and advancing to more complex and realistic configurations: a one-dimensional Ginzburg-Landau equation with an n-periodic growth potential (Sec. III A), a periodic array of interacting Bickley wakes (Sec. III B), and incompressible flow through an array of compressor blades (Sec. III C). In each application, particular attention is directed towards low-frequency organized motion and synchronization across multiple subunits, which is contrasted to flow behavior periodic over one single unit. Finally, Sec. IV presents conclusions, extensions, and an outlook for future applications.

II. MATHEMATICAL FRAMEWORK

We consider a general, nonlinear evolution problem of the form

$$\frac{\partial \mathbf{Q}}{\partial t} = \mathbf{f}(x,y,z,t;\mathbf{Q}), \tag{1}$$

where $\mathbf{Q}$ is a vector field that fully describes the state of our fluid system. We further assume periodicity over n identical units, which we representatively take in the z coordinate. This periodicity is mathematically expressed in the form $\mathbf{f}(x,y,z,t;\mathbf{Q}) = \mathbf{f}(x,y,z + n\ell,t;\mathbf{Q})$, with ℓ as the z extent of a single unit. After spatially discretizing the above equations and linearizing about an equilibrium point $\bar{\mathbf{Q}}$, with $\mathbf{Q} = \bar{\mathbf{Q}} + \varepsilon\mathbf{q}$, we arrive, for $O(\varepsilon)$, at an evolution equation for the small perturbations $\mathbf{q}$, which reads

$$\frac{d}{dt}\mathbf{q} = \mathsf{A}\mathbf{q}, \tag{2}$$

with $\mathsf{A} = \partial\mathbf{f}/\partial\mathbf{Q}|_{\bar{\mathbf{Q}}}$ associated with (1). The specific n-periodic shape of the governing equations (1) results in a block-circulant form of the Jacobian A with

$$\frac{d}{dt}\begin{pmatrix} \mathbf{q}_0 \\ \mathbf{q}_1 \\ \vdots \\ \mathbf{q}_{n-2} \\ \mathbf{q}_{n-1} \end{pmatrix} = \underbrace{\begin{pmatrix} \mathsf{A}_0 & \mathsf{A}_1 & \cdots & \mathsf{A}_{n-2} & \mathsf{A}_{n-1} \\ \mathsf{A}_{n-1} & \mathsf{A}_0 & \cdots & \mathsf{A}_{n-3} & \mathsf{A}_{n-2} \\ \mathsf{A}_{n-2} & \mathsf{A}_{n-1} & \cdots & \mathsf{A}_{n-4} & \mathsf{A}_{n-3} \\ \vdots & \vdots & & \vdots & \vdots \\ \mathsf{A}_1 & \mathsf{A}_2 & \cdots & \mathsf{A}_{n-1} & \mathsf{A}_0 \end{pmatrix}}_{\mathsf{A}} \underbrace{\begin{pmatrix} \mathbf{q}_0 \\ \mathbf{q}_1 \\ \vdots \\ \mathbf{q}_{n-2} \\ \mathbf{q}_{n-1} \end{pmatrix}}_{\mathbf{q}}. \tag{3}$$

In this expression, the discretized state vector $\mathbf{q}$ is partitioned into n components $\mathbf{q}_j$, $j = 0, \ldots, n - 1$, each fully describing the flow in the jth unit. By formulating the linearized problem in the form (3), we have tacitly assumed a coloring scheme for the state vector $\mathbf{q}$ that aligns all variables unit

by unit and identically from unit to unit. Depending on the original formulation of (1) or the chosen time-stepping scheme, an appropriate permutation of the state-vector variables may be required to bring the associated linearized system matrix A into block-circulant form; examples will be given in later sections.

It is important to note that the formulation (3) allows interactions between a given unit j with *any* of the remaining units $i \neq j$. The matrix $\mathsf{A}_0 \in \mathbb{C}^{N \times N}$, along the diagonal of A, describes the dynamics within the specific unit and is identical for each unit; the matrices $\mathsf{A}_{1,\dots,n-1} \in \mathbb{C}^{N \times N}$, in the off-diagonal positions of A, represent the interaction with the other units. The number of degrees of freedom in each subunit is denoted by N (commonly, the number of grid points times the number of state variables). Owing to the n-periodic configuration, the global matrix A is block circulant. This specific shape will have consequences on the analysis and simulation of n-periodic fluid systems and will be further exploited in the following sections.

First and foremost, we are interested in bringing the block-circulant matrix A into block-diagonal form. Recalling that block-circulant matrices represent special cases of block-Toeplitz matrices whose spectrum can be described by its associated symbol [25], we form the matrix $\mathsf{J} \in \mathbb{C}^{n \times n}$ defined as $\mathsf{J}_{j+1,k+1} = \rho_j^k / \sqrt{n}$, with $j,k = 0, 1, \dots, n-1$, and ρ_j as the nth roots of unity according to

$$\rho_j = \exp(ij\vartheta) \quad \text{with } \vartheta = \frac{2\pi}{n}, \quad j = 0, 1, \dots, n-1. \tag{4}$$

Based on the matrix J, we compose the unitary matrix $\mathsf{P} \in \mathbb{C}^{nN \times nN}$ according to

$$\mathsf{P} = \mathsf{J} \otimes \mathsf{I}_{N \times N}, \tag{5}$$

where $\otimes$ denotes the Kronecker product of two matrices and $\mathsf{I}_{N \times N}$ stands for the $N \times N$ identity matrix. With these definitions, it can easily be shown [26,27] that a similarity transformation based on P block diagonalizes the block-circulant matrix A according to

$$\mathsf{P}^H \mathsf{A} \mathsf{P} = \begin{pmatrix} \hat{\mathsf{A}}_0 & & & \\ & \hat{\mathsf{A}}_1 & & \\ & & \ddots & \\ & & & \hat{\mathsf{A}}_{n-1} \end{pmatrix} \equiv \hat{\mathsf{A}}, \tag{6}$$

with $\hat{\mathsf{A}}_j \in \mathbb{C}^{N \times N}$ denoting the decoupled subsystem matrices and the superscript H representing the transconjugate (Hermitian) operation. More importantly, this expression can be employed to efficiently evaluate any matrix function $f(\mathsf{A})$ for a block circulant A. We have

$$\mathsf{P}^H f(\mathsf{A}) \mathsf{P} = \begin{pmatrix} f(\hat{\mathsf{A}}_0) & & & \\ & f(\hat{\mathsf{A}}_1) & & \\ & & \ddots & \\ & & & f(\hat{\mathsf{A}}_{n-1}) \end{pmatrix} = f(\hat{\mathsf{A}}), \tag{7}$$

which will be helpful in forming various matrix operators arising in the temporal and frequential analysis of n-periodic fluid systems (see below).

We can already state at this point that the evaluation of matrix functions, a key component in the analysis of fluid systems, has been reduced to a corresponding and independent analysis of n smaller subsystem matrices $\hat{\mathsf{A}}_{0,\dots,n-1}$ by exploiting the block-circulant structure of the global system matrix A. It is interesting to point out that only $\lfloor \frac{n}{2} \rfloor$, rather than n, computations are necessary, if the coupling matrices $\mathsf{A}_{j \neq 0}$ satisfy a symmetry condition of the form

$$\mathsf{A}_j^H = \mathsf{A}_{n-j}, \quad j = 1, \dots, n-1. \tag{8}$$

In this case, the influence of neighboring subunits on each side of the central unit is equal. The symmetry condition (8) is often encountered in physical systems and is worth exploiting for computational efficiency.

In the preceding section and in what follows, we use the following notation for our system matrices: Matrices associated with the full n-periodic (global) system will be denoted simply by a symbol, e.g., the matrix A; the various blocks of this block-circulant matrix will be denoted by a subscript j, such as in A_j; once brought into block diagonal form via the matrix P, the transformed matrix will be marked by a caret, such as $\hat{\mathsf{A}}$, and its diagonal blocks will be indicated by $\hat{\mathsf{A}}_j$.

A. Modal solutions of the global matrix

A first step in our analysis is the assessment of the asymptotic ($t \to \infty$) stability of the global system matrix A, given by its spectrum. The block diagonalization from the preceding section suggests the spectral analysis of the diagonal blocks $\hat{\mathsf{A}}_j$, which can be accomplished independently and in parallel. The unitary similarity transformation (5) based on P is equivalent to the expression

$$\hat{\mathsf{A}}_j = \mathsf{A}_0 + \rho_j \mathsf{A}_1 + \rho_j^2 \mathsf{A}_2 + \cdots + \rho_j^{n-1} \mathsf{A}_{n-1} \tag{9}$$

for the decoupled subsystem matrices $\hat{\mathsf{A}}_j$ with the root-of-unity factor ρ_j introduced in (4) [28]. The spectrum of the global stability matrix A is then simply the union of the n spectra of $\hat{\mathsf{A}}_j$ for $j = 0, \ldots, n-1$.

By repeated multiplication by ρ_j of the eigenvalue problem associated with (3), it is not difficult to show that the compound vector of the form

$$\tilde{\mathbf{q}} = \begin{pmatrix} \mathbf{v}_j \\ \rho_j \mathbf{v}_j \\ \rho_j^2 \mathbf{v}_j \\ \vdots \\ \rho_j^{n-1} \mathbf{v}_j \end{pmatrix}, \quad j = 0, \ldots, n-1, \tag{10}$$

constitutes an eigenvector of $\mathsf{A} \in \mathbb{C}^{nN \times nN}$, i.e.,

$$\mathsf{A}\tilde{\mathbf{q}} = \tilde{\lambda}\tilde{\mathbf{q}}, \tag{11}$$

provided that the vector $\mathbf{v}_j \in \mathbb{C}^N$ in (10) satisfies the smaller ($N \times N$) eigenvalue problem, involving the subsystem matrices $\hat{\mathsf{A}}_j$,

$$\hat{\mathsf{A}}_j \mathbf{v}_j = \lambda \mathbf{v}_j. \tag{12}$$

The geometric sequence for the eigenvector components, starting with a fundamental solution $\mathbf{v}_j$, is equivalent to the underlying assumption of Bloch wave analysis.

We thus have a procedure to compute the full global spectrum without forming or decomposing the full global stability matrix A. For a given number n of identical subunits, we start by computing the nth roots of unity ρ_j, $j = 0, \ldots, n-1$. For each of these roots, we form the matrix $\hat{\mathsf{A}}_j$ following (9) and solve for its eigenvalues $\Lambda_j = \mathrm{diag}\{\lambda_1, \ldots, \lambda_N\}$ and eigenvectors $\mathsf{V}_j = \{\mathbf{v}_1, \ldots, \mathbf{v}_N\}$. We then form the global eigenvectors $\tilde{\mathbf{q}}$ from each $\mathbf{v}_{1,\ldots,N}$ according to (10); the eigenvalues $\lambda_{1,\ldots,N}$ for our specific value of ρ_j are already part of the global spectrum. As we repeat this procedure for all remaining roots of unity ρ_j, we recover the full global spectrum of A. However, only eigenvalue problems of the size of *one* individual unit (with N degrees of freedom) have to be solved, albeit multiple times. For large-scale applications, this latter feature becomes advantageous in a massively parallel computing environment. The analysis of a single subunit with periodic boundary conditions amounts to an analysis of the stability matrix $\hat{\mathsf{A}}_0$ with $\rho_0 = 1$, i.e.,

$$\hat{\mathsf{A}}_0 = \sum_{i=1}^{n} \mathsf{A}_i. \tag{13}$$

Before proceeding it is important to recall that circulant matrices have orthogonal eigenvectors and are thus normal [25]. Consequently, the norm of any matrix function is determined by the least-stable eigenvalue. For block-circulant matrices, as in our case, transient effects can arise due to non-normality of each individual subunit dynamics, but no additional transient effects arise from the superposition of different values of ρ_j as the eigenvectors of block-circulant matrices are block orthogonal. This latter statement can easily be verified by forming the scalar product of two eigenvectors of the form (10). We assume that the two eigenvectors stem from two different values of ρ, which we take as ρ_j and ρ_k with $j \neq k$. Denoting by $\mathbf{v}_j$ an eigenvector of $\hat{\mathsf{A}}_j$ and by $\mathbf{v}_k$ an eigenvector of $\hat{\mathsf{A}}_k$ we arrive at

$$\tilde{\mathbf{q}}_j^H \mathsf{Q} \tilde{\mathbf{q}}_k = \begin{pmatrix} \mathbf{v}_j \\ \rho_j \mathbf{v}_j \\ \rho_j^2 \mathbf{v}_j \\ \vdots \\ \rho_j^{n-1} \mathbf{v}_j \end{pmatrix}^H \begin{pmatrix} \mathsf{Q}_0 & & & \\ & \mathsf{Q}_0 & & \\ & & \ddots & \\ & & & \mathsf{Q}_0 \end{pmatrix} \begin{pmatrix} \mathbf{v}_k \\ \rho_k \mathbf{v}_k \\ \rho_k^2 \mathbf{v}_k \\ \vdots \\ \rho_k^{n-1} \mathbf{v}_k \end{pmatrix} \tag{14a}$$

$$= (1 + \xi + \xi^2 + \cdots + \xi^{n-1}) \mathbf{v}_j^H \mathsf{Q}_0 \mathbf{v}_k \tag{14b}$$

$$= \frac{1 - \xi^n}{1 - \xi} \mathbf{v}_j^H \mathsf{Q}_0 \mathbf{v}_k, \tag{14c}$$

with $\xi = \rho_j^* \rho_k = \exp[2\pi i(k - j)/n]$ and Q_0 representing a positive-definite weight matrix defined over one subunit with $\mathsf{Q} = \mathrm{diag}\{\mathsf{Q}_0, \ldots, \mathsf{Q}_0\}$. Recalling that $\xi^n = 1$ for $j \neq k$, we conclude that two global eigenvectors corresponding to two different root-of-unity values are mutually Q_0 orthogonal. This eigenvector structure for block-circulant matrices A will be important for the nonmodal analysis in the next section.

B. Nonmodal solutions of the global matrix

Even though a spectral analysis of the n-periodic system gives insight into long-time stability properties, we are even more interested in the short- or finite-time dynamics that arises from a superposition of modal solutions. Two cases emerge: (i) the superposition of modal solutions within a single subunit, governed by the eigenstructure of $\hat{\mathsf{A}}_j$, and (ii) the superposition of modal solutions from *all* subunits, taking into account the eigenstructures of $\hat{\mathsf{A}}_j$, $j = 0, \ldots, n - 1$. The latter case is of particular interest, as it may describe the cross-unit dynamics, which is absent in the former case.

A nonmodal analysis avoids the assumption of an exponential time dependence $\exp(\lambda t)$ and instead considers the initial-value problem (2) or its driven counterpart [29]. We have

$$\frac{d}{dt}\mathbf{q} = \mathsf{A}\mathbf{q}, \quad \frac{d}{dt}\mathbf{q} = \mathsf{A}\mathbf{q} + \mathbf{f},$$
$$\mathbf{q}(0) = \mathbf{q}_0, \quad \mathbf{q}(0) = \mathbf{0}. \tag{15}$$

We define the maximum amplification $G(t)$ and the optimal frequency response $R(\omega)$ as

$$G(t) = \max_{\mathbf{q}_0} \frac{\|\mathbf{q}(t)\|}{\|\mathbf{q}_0\|} = \|\exp(t\mathsf{A})\|, \quad R(\omega) = \max_{\hat{\mathbf{f}}} \frac{\|\hat{\mathbf{q}}\|}{\|\hat{\mathbf{f}}\|} = \|(i\omega\mathsf{I} - \mathsf{A})^{-1}\|, \tag{16}$$

with $\mathbf{f} = \hat{\mathbf{f}} \exp(i\omega t)$ and analogously for $\hat{\mathbf{q}}$. The matrix exponential norm determines the optimal amplification (in the chosen norm), starting from an optimal initial condition, over a user-defined time horizon $[0, t]$. The resolvent norm, in contrast, measures the optimal response (again, based on the chosen norm) to a harmonic forcing at a given frequency ω; the spatial shape of the optimal driving is given by $\hat{\mathbf{f}}$. Either analysis captures effects due to a potential nonorthogonality of the eigenvector structure or, equivalently, the non-normality of the underlying linearized evolution operator A.

In general, we have to evaluate the norm of a matrix function $\| f(\mathsf{A}) \|$ [either $f(z) = \exp(tz)$ or $f(z) = (i\omega - z)^{-1}$ in our case] for block-circulant arguments A. An eigenvalue decomposition of A, using its block-circulant structure, will be used to accomplish this. First, we recall the weight matrix $\mathsf{Q}_0 \in \mathbb{R}^{N \times N}$, defined identically over each subunit, which expresses a particular, and physically meaningful, measure of state-vector size, as well as the matrix $\mathsf{Q} = \mathrm{diag}\{\mathsf{Q}_0, \ldots, \mathsf{Q}_0\}$ as the block-diagonal matrix consisting of the n individual weight matrices Q_0. The latter matrix is used to express the norm of the global state vector according to $\|\mathbf{q}\|_\mathsf{Q}^2 = \mathbf{q}^H \mathsf{Q} \mathbf{q}$. This weighted vector norm induces the corresponding matrix norm as follows: The positive-definite matrix Q_0 is Cholesky decomposed into $\mathsf{Q}_0 = \mathsf{F}_0^H \mathsf{F}_0$ and block-diagonal matrices are formed according to $\mathsf{F} = \mathrm{diag}\{\mathsf{F}_0, \ldots, \mathsf{F}_0\}$ and $\mathsf{F}^{-1} = \mathrm{diag}\{\mathsf{F}_0^{-1}, \ldots, \mathsf{F}_0^{-1}\}$. The global matrix norm, applied to $f(\mathsf{A})$, is then given as $\| f(\mathsf{A}) \|_\mathsf{Q} = \| \mathsf{F} f(\mathsf{A}) \mathsf{F}^{-1} \|_2$, with the subscript 2 indicating the standard 2-norm [30]. We proceed by bringing the global matrix function of the block-circulant A into block-diagonal form using the unitary transformation P as introduced in (5). We then deduce for the (weighted) Q-norm of the global matrix function $f(\mathsf{A})$,

$$\| f(\mathsf{A}) \|_\mathsf{Q} = \| \mathsf{F}\mathsf{P} f(\hat{\mathsf{A}}) \mathsf{P}^H \mathsf{F}^{-1} \|_2 = \max_j \left\| \mathsf{F}_0 \mathsf{V}_j f(\Lambda_j) \mathsf{V}_j^{-1} \mathsf{F}_0^{-1} \right\|_2, \quad j = 0, \ldots, n-1. \quad (17)$$

The eigenvalues and eigenvectors in (17) satisfy $\hat{\mathsf{A}}_j \mathsf{V}_j = \mathsf{V}_j \Lambda_j$. The rightmost expression in (17) contains only matrices that are defined on a subunit and Eq. (17) thus states that the Q-weighted norm of the global matrix function is simply the maximum over all subunit matrix-norm calculations. This general expression can now be applied to $f(\mathsf{A}) = \exp(t\mathsf{A})$ to treat initial-value problems or to $f(\mathsf{A}) = (i\omega - \mathsf{A})^{-1}$ to investigate harmonically driven systems.

Besides the maximum energy amplification of an initial condition or the maximum energy response due to harmonic forcing, we are often interested in the shapes of the optimal initial and terminal conditions or, more importantly, the shapes of the optimal forcing and excited response. For linear time-invariant problems, this computation is often performed by a singular-value decomposition of the matrix exponential (evaluated at a given time t_*) or the resolvent norm (evaluated at a given frequency ω_*). As before, we can take advantage of the block-circulant structure of the underlying matrix and apply the singular-value decomposition (or, parenthetically, any other matrix decomposition) of $f(\mathsf{A})$ to each of the n blocks $f(\hat{\mathsf{A}}_j)$ individually, taking into account the weighting by the matrices F_0 and F_0^{-1}. Introducing the singular-value decomposition of the decoupled blocks as $\mathsf{U}_j \Sigma_j \mathsf{W}_j^H = \mathrm{svd}[\mathsf{F}_0 f(\hat{\mathsf{A}}_j) \mathsf{F}_0^{-1}]$, we can cast the principal left and right singular vectors $\mathbf{u}$ and $\mathbf{w}$ of the (global) matrix $f(\mathsf{A})$ in the form

$$\mathbf{u} = \begin{pmatrix} \mathbf{u}_j \\ \rho_j \mathbf{u}_j \\ \rho_j^2 \mathbf{u}_j \\ \vdots \\ \rho_j^{n-1} \mathbf{u}_j \end{pmatrix}, \quad \mathbf{w} = \begin{pmatrix} \mathbf{w}_j \\ \rho_j \mathbf{w}_j \\ \rho_j^2 \mathbf{w}_j \\ \vdots \\ \rho_j^{n-1} \mathbf{w}_j \end{pmatrix}, \quad (18)$$

with $\mathbf{u}_j$ and $\mathbf{w}_j$ as the principal left and right singular vectors of $f(\hat{\mathsf{A}}_j)$ and j chosen as $j = \arg\max_j \sigma_j$, with σ_j the largest singular value of Σ_j. In other words, we select j as the index that yields the largest norm (maximum singular value) of $f(\hat{\mathsf{A}}_j)$ over all its values $j = 0, \ldots, n-1$. The above expressions then provide a procedure to compute the optimal perturbation and the optimal frequency response of the *global* n-periodic system by solving for the principal singular vectors of the n *local* subsystems. Moreover, the computations for the n subsystems are independent and can be readily parallelized.

C. Input-output analysis and cross-unit dynamics

It is often advantageous and instructive to assess the input-output behavior of a complex system. To this end, forcing is applied only to a specific subdomain of the flow or to only a particular state variable; likewise, only limited and user-specified output quantities are measured and assessed. In this manner, the strength and characteristics of a link between an input and output quantity can be probed, leading to more physical insight into the fluid system [31]. For example, the influence of fuel-mixture fluctuations in the feed pipe on the acoustic far-field output of a premixed flame could be quantified, to name a representative case from combustion dynamics for this type of analysis.

Within our block-circulant analysis framework, we are interested in evaluating the general expression, formulated for the global system,

$$K = \|\mathsf{C} f(\mathsf{A}) \mathsf{B}\|_{\mathsf{Q}}, \tag{19}$$

where B and C represent masking matrices that select and construct specific input and output quantities, respectively, from the global state vector. The matrix function $f(\mathsf{A})$ is linked to either an initial-value problem (via a fundamental solution operator or, for a linear time-invariant system, a matrix exponential) or a driven problem (see above). Exploiting the block-circulant structure of A, we can bring the global matrix function into block-diagonal form using (5). We can write

$$K = \|\mathsf{FCP} f(\hat{\mathsf{A}}) \mathsf{P}^H \mathsf{B} \mathsf{F}^{-1}\|_2, \tag{20}$$

with $\hat{\mathsf{A}} = \mathrm{diag}\{\hat{\mathsf{A}}_0, \dots, \hat{\mathsf{A}}_{n-1}\}$. At this stage we will be more specific and investigate the perturbation propagation across subunits by choosing the block-diagonal masking matrices B and C to be nonzero in a specific subunit and zero elsewhere. More specifically, we study the dynamics between the single (input) subunit p and the single (output) subunit q. Within these subunits we introduce the local masking matrices as $\mathsf{B}_p \in \mathbb{C}^{N \times N}$ and $\mathsf{C}_q \in \mathbb{C}^{N \times N}$, respectively. The global masking matrices (in block-diagonal notation) are then given as

$$\mathsf{B} = \begin{pmatrix} \mathsf{0}_{p-1} & & \\ & \mathsf{B}_p & \\ & & \mathsf{0}_{n-p} \end{pmatrix}, \quad \mathsf{C} = \begin{pmatrix} \mathsf{0}_{q-1} & & \\ & \mathsf{C}_q & \\ & & \mathsf{0}_{n-q} \end{pmatrix}, \tag{21}$$

where $\mathsf{0}_k$ denotes a $kN \times kN$ matrix of zeros. We further recall the definition (5) of the matrix P in terms of a Kronecker product, which allows a more explicit formulation of $\mathsf{P}^H \mathsf{B}$ and CP by considering only nonzero contributions. We introduce the notation $\mathsf{M}_{:,p}$ and $\mathsf{M}_{q,:}$ to denote the pth block column or qth block row of a matrix M consisting of $n \times n$ blocks of size $N \times N$. We have

$$(\mathsf{P}^H \mathsf{B})_{:,\neq p} = \mathsf{0}_1, \quad (\mathsf{P}^H \mathsf{B})_{:,p} = \mathsf{B}_p \big(\rho_k^{p-1}\big)^* / \sqrt{n}, \quad k = 0, \dots, n-1 \tag{22a}$$

$$(\mathsf{CP})_{\neq q,:} = \mathsf{0}_1, \quad (\mathsf{CP})_{q,:} = \mathsf{C}_q \rho_{q-1}^k / \sqrt{n}, \quad k = 0, \dots, n-1. \tag{22b}$$

Substituting expression (22b) into (20) yields the compact formula for the norm of a function $f(z)$, describing the transunit dynamics between unit p and q, according to

$$K_{pq} = \|\mathsf{FCP} f(\hat{\mathsf{A}}) \mathsf{P}^H \mathsf{B} \mathsf{F}^{-1}\|_2 = \left\| \mathsf{F}_0 \mathsf{C}_q \left(\frac{1}{n} \sum_{j=0}^{n-1} \zeta_j f(\hat{\mathsf{A}}_j) \right) \mathsf{B}_p \mathsf{F}_0^{-1} \right\|_2, \tag{23}$$

with $\zeta_j = \exp[2\pi i j (q - p)/n]$. As before, the final expression contains only components that describe single-unit characteristics; they can be evaluated efficiently and independently. At the same time, global effects spanning multiple units are captured by the above formula.

D. Direct-adjoint analysis

The previous algorithms for the computation of optimal initial condition and frequency response, using the respective matrix function $f(\mathsf{A})$, via a singular-value decomposition holds for linear

time-invariant systems. Deviating from this restriction requires a more general approach, commonly involving direct and adjoint equations [29]. In this approach, we state a cost functional $\mathcal{J}$ to be optimized, such as optimal energy amplification, maximal response to forcing or optimal suppression of instabilities, among many other options. In general, the cost functional depends on the (global) state vector $\mathbf{q}$ and a control variable $\mathbf{f}$ (e.g., modeling boundary forcing); mathematically, we have $\mathcal{J} = \mathcal{J}(\mathbf{q}, \mathbf{f})$. Our optimization problem $\mathcal{J} \to$ opt is constrained by our governing equation (3), which we augment on the left by $\mathbf{f}$, which represents the application of control efforts. It can then be restated as an unconstrained problem by introducing Lagrange multipliers or adjoint variables, denoted by $\mathbf{q}^+$, which will enforce the constraint from our governing equation. We obtain an augmented Lagrangian $\mathcal{L}$ in the form

$$\mathcal{L}(\mathbf{q}, \mathbf{q}^+, \mathbf{f}) = \mathcal{J}(\mathbf{q}, \mathbf{f}) - \left\langle \mathbf{q}^+, \frac{d}{dt}\mathbf{q} - A\mathbf{q} - \mathbf{f} \right\rangle, \tag{24}$$

with $\langle \mathbf{f}_1, \mathbf{f}_2 \rangle = \int_0^T \mathbf{f}_1^H \mathbf{f}_2 \, dt$ as the chosen inner product. Rendering zero the first variations of $\mathcal{L}$ with respect to $\mathbf{q}$, $\mathbf{q}^+$, and $\mathbf{f}$, respectively, results in a system of three equations

$$\frac{d}{dt}\mathbf{q} = A\mathbf{q} + \mathbf{f}, \quad -\frac{d}{dt}\mathbf{q}^+ = A^H \mathbf{q}^+ + \frac{\delta \mathcal{J}}{\delta \mathbf{q}}, \quad \frac{\delta \mathcal{J}}{\delta \mathbf{f}} = \mathbf{q}^+. \tag{25}$$

The first of Eqs. (25) restates our original governing system, while the second represents an evolution equation for the adjoint variable $\mathbf{q}^+$. The third of Eqs. (25) produces an expression for the gradient of our cost functional $\mathcal{J}$ with respect to the control variable $\mathbf{f}$ and is referred to as the optimality condition. These three equations need to be satisfied for an optimal solution. Instead of solving the system of equations (25) simultaneously, we employ an iterative scheme: Starting with an initial guess for $\mathbf{f}$, we solve the direct and adjoint equations in (25); the resulting solution is used to evaluate the optimality condition and, via the gradient expression, determine an improved guess for $\mathbf{f}$ for a subsequent iteration. The iterative scheme terminates after a user-defined convergence criterion is satisfied. For further details on the algorithmic steps, the reader is referred to [29] or [32].

Again, taking advantage of the block-circulant structure of A and A^H, we can decouple the subunits by using the transformation P from (5). Applying this transformation, we arrive at a system of three equations, the direct and adjoint evolution equation and the optimality condition, for each of our subunits. We obtain

$$\frac{d}{dt}\mathbf{q}_j = \hat{A}_j \mathbf{q}_j + \mathbf{f}_j, \quad -\frac{d}{dt}\mathbf{q}_j^+ = \hat{A}_j^H \mathbf{q}_j^+ + \frac{\delta \mathcal{J}}{\delta \mathbf{q}_j}, \quad \frac{\delta \mathcal{J}}{\delta \mathbf{f}_j} = \mathbf{q}_j^+, \tag{26}$$

with $(\mathbf{f}_0, \ldots, \mathbf{f}_{n-1}) = P^H \mathbf{f}$. As before, these systems are best treated iteratively: The direct and adjoint evolution equations are solved for a given control $\mathbf{f}_j$ (a guess for the first iteration), after which the gradient expression is used to update or improve the control $\mathbf{f}_j$ for the next iteration. Once more, the global problem breaks down into n local problems, which can be solved independently.

E. Implementation for large-scale applications

The computational formalism for the analysis of *n*-periodic fluid systems based on the spectral properties of block-circulant matrices has been formulated for a first-order temporal evolution problem. Time discretization by higher-order stepping schemes, however, typically introduces multiple time levels of state vector. In this case, the corresponding spectral problem is polynomial in the eigenvalue and the solution algorithm for the eigenvalues and eigenvectors has to be adjusted accordingly [33,34]. It also has to be kept in mind that, in this case, the state vector has to be reordered to yield a unit-by-unit composition; the same reordering will bring the global system matrices into block-circulant form. An example where this modification is necessary is included below (see Sec. III C).

For large-scale problems, the linearization step resulting in (2) can most conveniently be accomplished using techniques such as the complex-step derivative [35] combined with a tiling
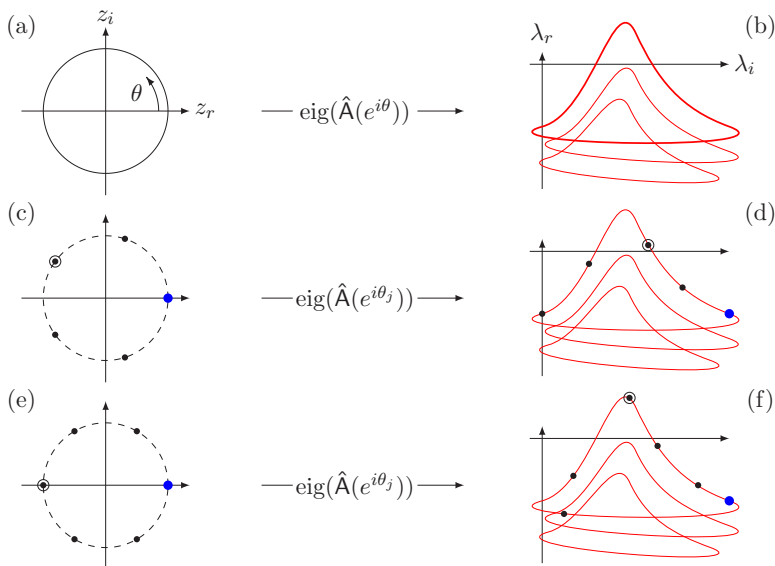
FIG. 2. Sketch of the spectrum of a block-circulant matrix. (a) and (b) The spectrum is continuously parametrized by θ and is given by the map of the unit circle under eig($\hat{\mathsf{A}}$); N curves (in our sketch, $N = 3$) result, with $\hat{\mathsf{A}} \in \mathbb{C}^{N \times N}$. (c) and (d) The spectrum for a 5-periodic configuration, with block matrices $\mathsf{A}_{0,1,n-1}$ as in (a) and (b), follows from a discretization of the continuous curve (only the dominant branch is shown). (e) and (f) Spectrum for a 6-periodic configuration, with block matrices $\mathsf{A}_{0,1,n-1}$ as in (a) and (b). Notice the increase in growth rate of the least-stable mode (circled symbol), as one more unit is added to the 5-periodic configuration. The eigenvalue corresponding to $\theta = 0$ is indicated in blue and is independent of the number n of subunits.

method based on the decoupling of grid points beyond the maximum stencil width [36]. Automatic differentiation techniques (see [37]) can also be applied to access linearized or adjoint information, as can alternative techniques (see, e.g., [38]).

The case of nearest-neighbor coupling is rather common in many applications. In this case, only a three-unit system needs to be discretized and processed, independent of the final configuration and periodicity of interest. In other words, only the system matrices A_0, A_1, and A_2 (from the 3-periodic system) have to be formed and stored. Stability and receptivity properties of different configurations with a *varying* number of subunits do not require additional computations beyond the initial three system matrices $\mathsf{A}_{0,1,2}$. Their superposition and weighting with ρ_j according to

$$\hat{\mathsf{A}}_j = \mathsf{A}_0 + \rho_j \mathsf{A}_1 + \mathsf{A}_2/\rho_j \tag{27}$$

determine the block-diagonalized subunit matrices $\hat{\mathsf{A}}_j$ that enter the expressions for the analysis of n-periodic systems given above. In more mathematical terms, the symbol curve is given as [25]

$$\hat{\mathsf{A}}(z) = \mathsf{A}_0 + z\mathsf{A}_1 + \mathsf{A}_2/z \tag{28}$$

for $z = \exp(i\theta)$ and $\theta \in [0, 2\pi]$, and θ-parametrized line spectra can be computed as eig$[\hat{\mathsf{A}}(\theta)]$. The spectra for specific n-periodic configurations consist simply of discretizations of the unit circle $\exp(i\theta)$ into n points, i.e., $\exp(i\theta_j)$ with $\theta_j = 2\pi j/n$, and a subsequent mapping onto the line spectra (see Fig. 2 for a sketch). In this manner, it is straightforward to quantify the sensitivity of spectral properties to the removal ($n \rightarrow n - 1$) or augmentation ($n \rightarrow n + 1$) by a subunit. Treating the change in n as a matrix perturbation problem for $\hat{\mathsf{A}}[\exp(i\theta)]$, we can link, to first order, a change in
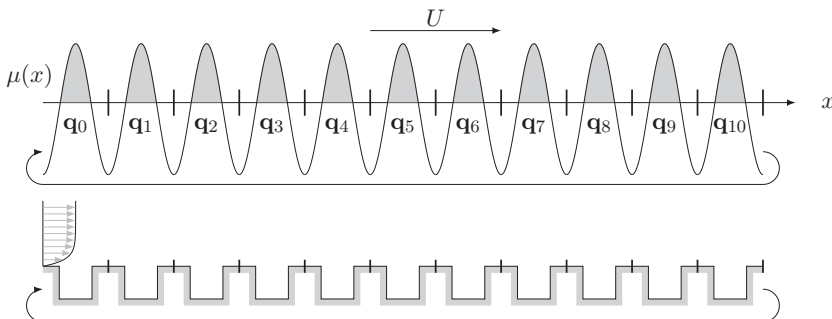
FIG. 3. Sketch of the 11-periodic potential (growth and decay function) used in the example of the Ginzburg-Landau equation, modeling the flow over a grooved wall (see the bottom). The remaining parameters are $U = 10$ and $\nu = 10^{-4}$. Each of the 11 subunits has been discretized by $N = 100$ mesh points.

θ to a change in an eigenvalue of $\hat{\mathsf{A}}$ according to

$$\delta\lambda_k = i\mathbf{w}_k^H[\mathsf{A}_1 \exp(i\theta) - \mathsf{A}_2 \exp(-i\theta)]\mathbf{v}_k\delta\theta, \tag{29}$$

where $\mathbf{w}_k$ and $\mathbf{v}_k$ denote the left and right eigenvectors, respectively, of $\hat{\mathsf{A}}[\exp(i\theta)]$ corresponding to the eigenvalue λ_k and satisfying the normalization condition $\mathbf{w}_k^H\mathbf{v}_k = 1$. For the special case of changing the number of subunits from n to $n + \Delta$, we obtain, for a user-defined root of unity j, the expression $\delta\theta_j/\theta_j = -\Delta/(n + \Delta)$. From the above we can determine, for example, the change in growth rate of the kth eigenvalue for a specific j by considering the real part of (29).

In an effort to encourage experimentation with the proposed computational framework and to facilitate the analysis of *n*-periodic fluid systems, the codes underlying the examples in this article (see Sec. III) will be made available, together with brief documentation [39].

III. APPLICATIONS

The methodology introduced above is now applied to *n*-periodic fluid systems of increasing complexity, starting from a simple model equation to the analysis of a 54-blade passage. In each subsection, various aspects of the formalism are demonstrated and special emphasis is directed towards effects stemming from a synchronization across multiple subunits and the description of lock-in processes.

A. A simple model: The Ginzburg-Landau equation with periodic potential

In this section we will consider the linearized Ginzburg-Landau equation with an *n*-periodic potential or growth function. This equation models physical processes commonly encountered in more complex fluid systems, such as convection, dissipation, dispersion, and localized amplification of perturbations. We have

$$\frac{\partial u}{\partial t} = -U\frac{\partial u}{\partial x} + \nu\frac{\partial^2 u}{\partial x^2} + \mu(x)u, \tag{30}$$

with U the advection speed, ν (potentially complex) viscosity, and $\mu = -\cos(2\pi x)$ the growth and decay function. We consider the interval $x \in [0,1]$ for each subunit, but align n such units before periodic boundary conditions link the nth unit back to the first one. The global problem thus spans the spatial interval $x \in [0,n]$. The continuous equation is discretized in space using finite differences, with $N = 100$ points per subunit interval. For the case presented below, we have chosen 11 identical subunits, i.e., $n = 11$ (see Fig. 3 for a sketch of the global growth and decay function). The remaining governing parameters are $U = 10$ and $\nu = 10^{-4}$. This configuration models, for example, shear flow over a grooved wall, where each shallow cavity acts as an amplifier of local instabilities. Of interest in
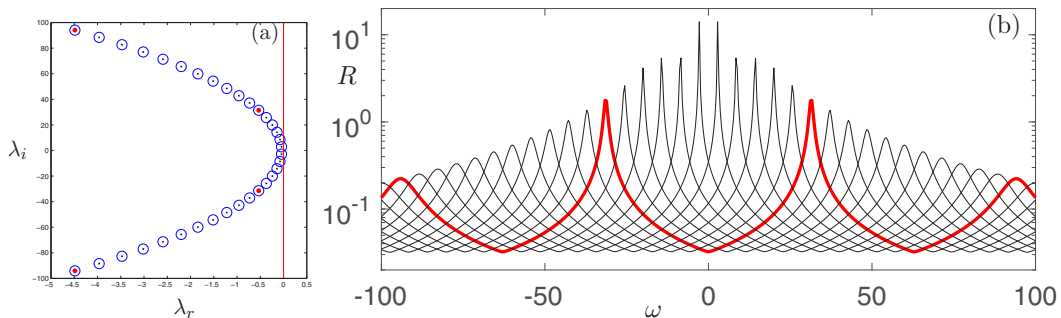
FIG. 4. Block-circulant complex Ginzburg-Landau system with $N = 100$ (discretization points per period), $\nu = 10^{-4}$, $U = 10$, and $\mu(x) = -\cos(2\pi x)$ with $x \in [0,1]$. Eleven periods have been considered ($n = 11$). (a) Spectrum of the Ginzburg-Landau operator. The blue and black symbols indicate the global spectrum, computed globally (blue circles) and using the root-of-unity formalism (black dots). The red symbols correspond to the 1-periodic system ($\rho_0 = 1$), where periodic boundary conditions are enforced over one single subunit. (b) Resolvent norm R versus the forcing frequency ω. The black curves stem from the analysis of the subsystems for different ρ_j. The maximum over all curves corresponds to the global 11-periodic solution. The red curve corresponds to the choice $\rho_0 = 1$.

this case is the global behavior of flow over an array of grooves, in particular the rise of synchronized motion linking multiple cavity units.

First, we compute the spectrum, illustrated in Fig. 4(a). It shows an eigenvalue distribution typical of an advection-diffusion equation. Marked in Fig. 4(a) are the eigenvalues of the global problem, i.e., the eigenvalues of A, in blue symbols; they have been included to validate the collective eigenvalues of the submatrices $\hat{\mathsf{A}}_j$, $j = 0, \ldots, 10$ (see the small black symbols). In addition, the eigenvalues of the matrix $\hat{\mathsf{A}}_0$ are included as red symbols. The latter eigenvalues represent the dynamics of the 1-periodic system: These eigenvalues result from considering a single subunit with periodic boundary conditions. We observe that the $\hat{\mathsf{A}}_0$ eigenvalues are more damped; the most-unstable modes of the system, however, do not belong to the spectrum of the 1-periodic system.

An even more striking picture emerges from considering the response of the global and 1-periodic system to external harmonic forcing [see Fig. 4(b)]. We observe strong pseudoresonance behavior for lower frequencies (e.g., $-20 \lesssim \omega \lesssim 20$), where the 1-periodic solution (in red) predicts an only modest response. We conclude that the inclusion of additional eigenvalues in the global spectrum is responsible for a slow-motion dynamics that spans and couples multiple subunits and thus is absent in the 1-periodic system.

B. An *n*-periodic array of wakes

Whereas the periodicity of the previous example has been in the coordinate direction that is aligned with the mean advection, we will next consider the effect of a transverse periodicity on the collective behavior of n identical subunits. Configurations with this type of multiple, but identical, unit are common in many fluid devices: Spray nozzles, fuel injection systems, heat exchangers, and screens are examples of this kind. Also, many geometric modifications to standard configurations, such as the chevron-type corrugations of engine nacelles in commercial airliners to reduce noise, introduce a transverse periodicity of the mean-flow profiles.

In an attempt to model transverse periodic arrays of fluid systems we consider the linear stability of a row of wakes, where each individual unit is modeled as a Bickley wake with a base profiles given by

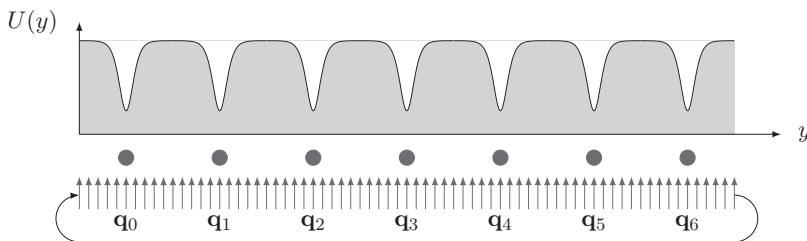$$U(y) = 1 - A \operatorname{sech}^2\left[a\left(y - \tfrac{1}{2}\right)\right], \tag{31}$$

FIG. 5. Sketch of a 7-periodic configuration of Bickley wakes.

with $0 \leqslant y \leqslant 1$. The parameter a controls the width of the wake; the parameter A determines the velocity deficit. Both parameters can be used to model the streamwise evolution of the wake profile behind bluff bodies. In the examples below, we select $a = 10$ and $A = 0.75$. A global configuration consisting of n linked subunits will be considered; a sketch of the configuration (for $n = 7$) is given in Fig. 5.

The temporal evolution of two-dimensional perturbations superimposed on this base flow is governed by the Orr-Sommerfeld equation given by

$$\lambda \left(\frac{d^2}{dy^2} - \alpha^2 \right) v = -i\alpha U \left(\frac{d^2}{dy^2} - \alpha^2 \right) v + i\alpha U'' v + \frac{1}{\mathrm{Re}} \left(\frac{d^2}{dy^2} - \alpha^2 \right)^2 v, \qquad (32)$$

with v the normal velocity, α the streamwise wave number, Re the Reynolds number based on the freestream velocity and the distance between the individual wakes, and λ the eigenvalue whose real part constitutes the exponential growth or decay rate. The perturbation is assumed in the form $v(y) \exp(i\alpha x) \exp(\lambda t)$. Formulating the stability problem for a global problem consisting of n subunits, a block-circulant global stability matrix results. As before, we are interested in contrasting the dynamics of perturbations over one subunit against the disturbance dynamics over multiple units. To this end, we deduce the entries in the block-circulant global matrix with nearest-neighbor coupling, i.e., A_0, A_1, and A_{n-1}, where A_0 describes the dynamics of the individual subunit, while A_1 and A_{n-1} account for the coupling to adjacent units. We use fourth-order compact difference schemes to discretize Eq. (32) in the cross-stream coordinate direction.

First, we choose a Reynolds number of Re $= 400$ and a streamwise wave number of $\alpha = 1$ and consider a configuration with three identical units. The spectrum is shown in Fig. 6(a) and indicates an asymptotic instability at these parameter values, with the least-stable eigenvalue at $\lambda = 0.0993 + 0.9012i$. The eigenvalues are colored by the index j with $j = 0$ (representing a fully periodic state $\rho_0 = 1$) in gray and $j = 1$ [representing a cross-unit periodicity $\rho_1 = \exp(2\pi i/3)$] in blue. We observe that the strongest instability is of the fully periodic type; a nearly neutral, multi-unit-periodic mode, at a higher phase velocity λ_i/α, is the second most-amplified mode. For higher modes the spectrum displays the typical Y shape of viscous shear flows: mean modes aligned with the average base-flow velocity ($\bar{U} \approx 0.82$), which divide the spectrum into slower and faster modes. Modes with different periodicity interlace.

Depicting the modal shapes of the first six least-stable modes gives more insight into the perturbation dynamics of the coupled three-wake configuration. This dynamic becomes more lucid by integrating streak lines based on the six separate normal-velocity fields to indicate the cross-stream displacement of the perturbations. To this effect, an equispaced (in the y direction) array of particles is released and tracked through the respective modal velocity field. The results are displayed in Fig. 7. For the least-stable mode [Fig. 7(a)], we observe a synchronized oscillatory motion of the wake, depicted over a full period given by the respective eigenvalue (and ignoring the small imaginary part). The next most-unstable mode [Fig. 7(b)], however, displays a nonsynchronized behavior where the three wakes repeatedly diverge from and converge towards the adjacent units. This break in cross-stream symmetry continues for the next mode [Fig. 7(c)], but returns to symmetry for the
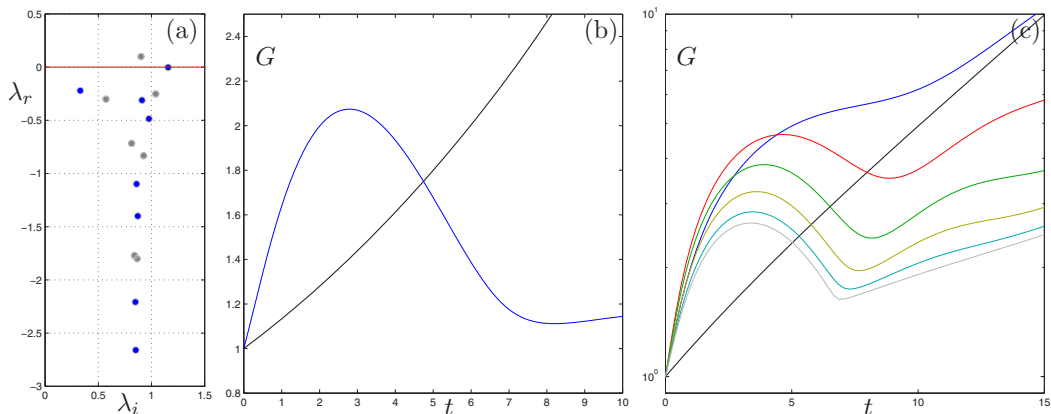
FIG. 6. (a) Spectrum of a three-unit configuration of Bickley wakes ($a = 10$ and $A = 0.75$) with $\alpha = 1$ and Re $= 400$: gray, $\rho_0 = 1$; blue, $\rho_1 = \exp(2\pi i/3)$. (b) Norm of the matrix exponential (maximal amplification) for the three-unit configuration. (c) Norm of the matrix exponential for a 13-unit configuration for $\alpha = 1$ and Re $= 400$ for ρ_j, $j = 0, \ldots, 6$.

fourth and fifth modes [Figs. 7(d) and 7(e)]. The sixth mode in this sequence [Fig. 7(f)] again shows unsynchronized subunits.

While our analysis of the modal structures identifies the strongest instability for a synchronized motion (i.e., a mode with $\rho_0 = 1$), the finite-time analysis based on the matrix exponential norm shows [Fig. 6(b)] that, for short times ($t \lesssim 4.5$), maximum amplification is achieved by an unsynchronized perturbation dynamics; for larger times ($t \gtrsim 4.5$), however, the synchronized motion prevails. The same graph demonstrates that unsynchronized transient amplification over two convective time units reaches energy levels that synchronized motion reaches only after more than six convective time units. Whether this disparity in amplification is sufficient for a selection principle and the observation of preferred (unsynchronized) structures requires additional consideration.

To further demonstrate the rise and importance of cross-unit motion, we extend the above analysis to a configuration with 13 units. This type of geometry may describe fluid motion past cylinder bundles or mesh screens. A modal analysis still confirms the least-stable mode as a synchronized mode [with $\rho_0 = 1$; see Fig. 8(a)]; the two subsequent modes, however, show the locking of adjacent
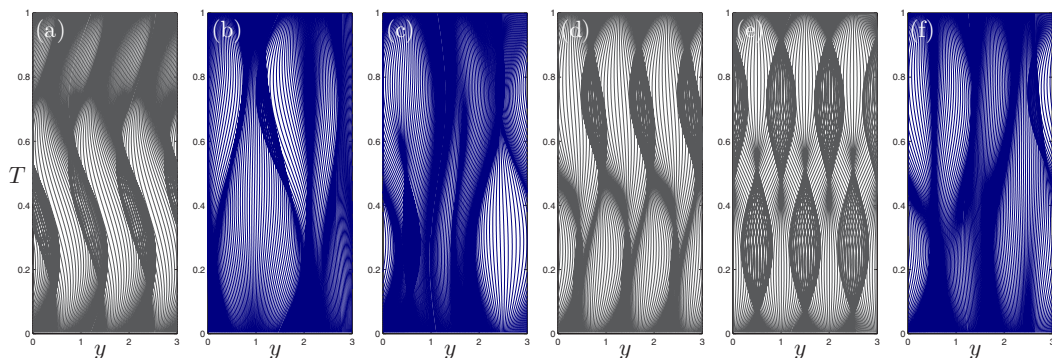

FIG. 7. Modal shapes of the first six least-stable modes of the three-wake configuration, visualized by streak lines integrated in the cross-stream velocity field: gray, synchronized motion for $\rho_0 = 1$; blue, unsynchronized motion for $\rho_1 = \exp(2\pi i/3)$. In all cases, a full period T, given by the respective phase velocity, is shown; the real part of the eigenvalue has been ignored in the computation of the streak lines.
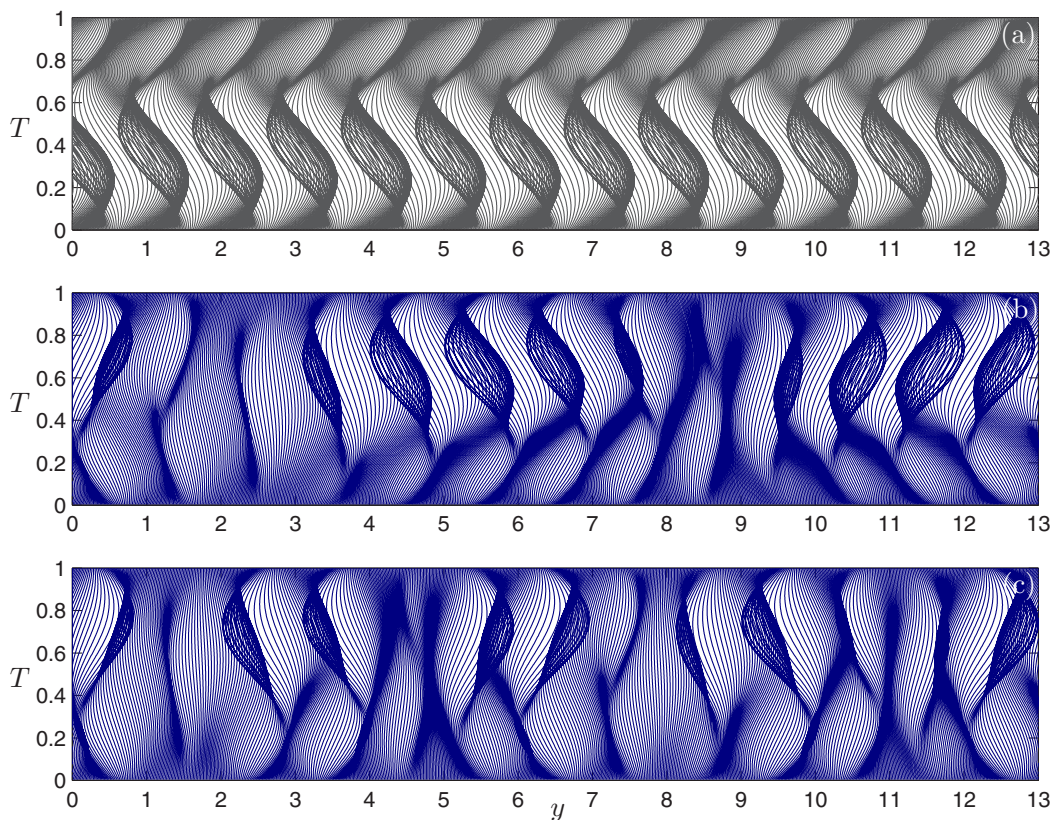
FIG. 8. Modal shapes of the first three least-stable modes of a 13-wake configuration, visualized by streak lines integrated in the cross-stream velocity field: gray, synchronized motion for $\rho_0 = 1$; blue, unsynchronized motion for $\rho_1 = \exp(2\pi i/13)$ and $\rho_2 = \exp(4\pi i/13)$. In all cases, a full period T, given by the respective phase velocity, is shown; the real part of the eigenvalue has been ignored in the computation of the streak lines.

units in groups [as displayed in Figs. 8(b) and 8(c) by streak lines]. The nonmodal analysis of the 13-wake configuration [Fig. 6(c)] based on the matrix exponential norm even more strongly asserts the fact that unsynchronized motion dominates the short-time dynamics of the 13-periodic array of Bickley wakes. For our parameter values, the perturbation energy amplification from synchronized motion dominates only after more than 15 convective time units.

In closing, we stress that, besides considering the above temporal stability problem for the periodic array of Bickley wakes, the corresponding spatial stability problem can be treated within the same framework. In this case, a fourth-degree polynomial eigenvalue problem for the complex streamwise wave number α can be formulated that, after an appropriate reordering of the global state vector $\mathbf{q}$, can be recast in block-circulant form.

C. Flow through a 54-periodic blade row

As a final example, we demonstrate the analysis of n-periodic fluid systems presented in this paper on a more complicated flow configuration of interest in turbomachinery applications. To this end, we consider the stability characteristics of incompressible flow through a periodic linear cascade.

Throughout this example we use a numerical solver for the two-dimensional Navier-Stokes equations that implements the projection-based immersed boundary method [40]. Based on this technique, the governing equations in nondimensional form formulated for a domain $\mathcal{D}$

read [41]

$$\frac{\partial \mathbf{u}}{\partial t} + \mathbf{u} \cdot \nabla \mathbf{u} = -\nabla p + \frac{1}{\text{Re}}\nabla^2 \mathbf{u} + \int_{\mathcal{C}} \mathbf{f}(s)\delta(\mathbf{x} - \xi(s))\, ds, \tag{33}$$

$$\nabla \cdot \mathbf{u} = 0, \tag{34}$$

$$\mathbf{u}[\xi(s)] = \int_{\mathcal{D}} \mathbf{u}(\mathbf{x})\delta(\xi(s) - \mathbf{x})\, d\mathbf{x} = \mathbf{u}_B(s), \quad s \in \mathcal{C}, \tag{35}$$

where the pressure p and the distributed momentum sources $\mathbf{f}(s)$ along the boundary of the obstacle $\mathcal{C}$ act as a set of Lagrange multipliers that enforce, respectively, the incompressibility constraint and the no-slip boundary condition. Equations (33)–(35) are discretized using a staggered-mesh finite-volume formulation; the viscous terms are discretized using the implicit Crank-Nicolson method, the advection terms are discretized using the explicit second-order Adams-Bashforth scheme, and the integrals involving the δ functions are discretized using a mollified δ function [42]. At this point, the flow field at a given time step $\mathbf{Q}^{k+1}$ and the value of the Lagrange multiplier λ are obtained from the flow fields at the two previous time steps, denoted by $\mathbf{Q}^k$ and $\mathbf{Q}^{k-1}$. Flow field boundary conditions $\mathbf{bc}_1$ and $\mathbf{bc}_2$ are imposed and the following system of equations is solved:

$$\begin{pmatrix} \mathsf{A} & \mathsf{Q} \\ \mathsf{Q}^T & 0 \end{pmatrix} \begin{pmatrix} \mathbf{Q}^{k+1} \\ \lambda \end{pmatrix} = \begin{pmatrix} \mathsf{B}\mathbf{Q}^k - \frac{3}{2}\mathcal{N}(\mathbf{Q}^k) + \frac{1}{2}\mathcal{N}(\mathbf{Q}^{k-1}) + \mathbf{bc}_1 \\ \mathbf{r}_2 \end{pmatrix}. \tag{36}$$

The reader is referred to [40] for the various definitions of the matrices A, B, and Q, the nonlinear function $\mathcal{N}(\cdot)$ and the vectors $\mathbf{bc}_1$, $\mathbf{bc}_2$, and $\mathbf{r}_2$.

We now consider a two-dimensional periodic linear cascade consisting of 54 NACA E^3 Rotor B airfoils (see [43,44] for a description of the blade geometry) with a pitch-to-chord ratio of $\sigma = H/C = 0.929\,36$ and a stagger angle of $56.6°$. The governing equations are then solved in the reference frame of the cascade; the velocity of the unperturbed incoming flow and the blade chord are taken, respectively, as the reference speed and reference length scale. The angle of attack, defined as the angle between the unperturbed incoming flow direction and the blade chord, is taken as $11.1°$ and the Reynolds number Re, based on chord, is 700. The computational domain for one blade passage is defined for $-6.56 \leqslant x \leqslant 6.56$ and $-0.465 \leqslant y \leqslant 0.465$. Upstream of the blade passages we impose a Dirichlet boundary condition for the velocity components, while a convective outflow boundary condition is implemented downstream. In the horizontal direction, the numerical grid is uniform for $-0.55 \leqslant x \leqslant 0.55$, with $\Delta x = 0.0036$, and is stretched upstream and downstream until the maximum spacing is $\Delta x = 0.03$; in the vertical direction the numerical grid has a constant spacing equal to $\Delta y = 0.0036$. The time step has been taken as $\Delta t = 0.0018$ and the resulting numerical grid has 766 cells in the horizontal direction and 258 cells per blade passage in the vertical direction.

Following the remark in Sec. II E about the efficient composition of the necessary matrices for nearest-neighbor configurations, we consider a three-blade passage to extract the subunit matrices required in our analysis.

First, the flow configuration presented above is found to be globally stable and the base flow $\bar{\mathsf{Q}}$, depicted in Fig. 9 by the vertical velocity component, has been computed simply by marching in time the governing equations from a given initial condition. Note that the base flow is periodic over one blade passage.

The above nonlinear equations are linearized about the base flow presented above, yielding the following system of linear equations for the temporal advancement of a small perturbation $\mathbf{q}$ over one time step:

$$\begin{pmatrix} \mathsf{A} & \mathsf{Q} \\ \mathsf{Q}^T & 0 \end{pmatrix} \begin{pmatrix} \mathbf{q}^{k+1} \\ \lambda \end{pmatrix} = \begin{pmatrix} (\mathsf{B} - \frac{3}{2}\mathsf{N})\mathbf{q}^k + \frac{1}{2}\mathsf{N}\mathbf{q}^{k-1} \\ \mathbf{0} \end{pmatrix}, \tag{37}$$
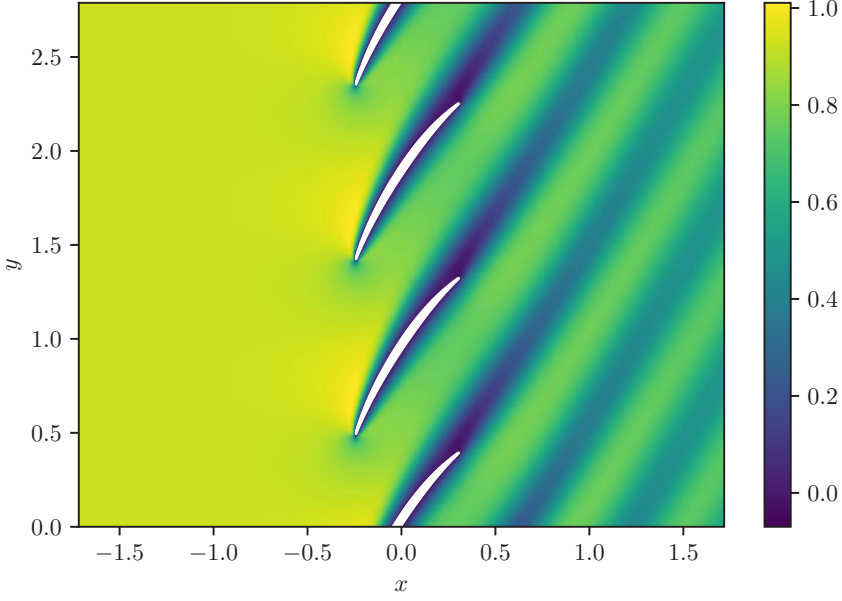
FIG. 9. Base flow for a linear cascade consisting of NACA E^3 Rotor B blade profiles with a pitch-to-chord ratio of $\sigma = H/C = 0.929\,36$ and a stagger angle of $56.6°$. The angle of attack is $11.1°$ and the chord-based Reynolds number is Re = 700. The flow is visualized by the vertical velocity component. See the text for details on the numerical grid.

where $\mathsf{N} = [\partial \mathcal{N}(\mathbf{Q})/\partial \mathbf{Q}]|_{\bar{\mathsf{Q}}}$ represents the linearized advection terms about the base flow $\bar{\mathsf{Q}}$. By introducing the definition

$$\tilde{\mathbf{x}}^k = \begin{pmatrix} \mathbf{q} \\ \lambda \end{pmatrix}^k, \quad \tilde{\mathsf{M}} = \begin{pmatrix} \mathsf{A} & \mathsf{Q} \\ \mathsf{Q}^T & 0 \end{pmatrix}, \quad \tilde{\mathsf{C}} = \begin{pmatrix} -\mathsf{B} + \frac{3}{2}\mathsf{N} & 0 \\ 0 & 0 \end{pmatrix}, \quad \tilde{\mathsf{K}} = \begin{pmatrix} -\frac{1}{2}\mathsf{N} & 0 \\ 0 & 0 \end{pmatrix}, \tag{38}$$

the temporal advancement over one time step reads

$$\tilde{\mathsf{M}}\tilde{\mathbf{x}}^{k+1} + \tilde{\mathsf{C}}\tilde{\mathbf{x}}^k + \tilde{\mathsf{K}}\tilde{\mathbf{x}}^{k-1} = 0. \tag{39}$$

Considering (38), we note that while the matrix entries $\mathsf{A}, \mathsf{Q}, \mathsf{B}$, and N are individually block circulant, the matrices $\tilde{\mathsf{M}}, \tilde{\mathsf{C}}$, and $\tilde{\mathsf{K}}$ are not. A final row reordering, which we introduce as a permutation G of a $3N \times 3N$ identity matrix, brings the state vector $\tilde{\mathbf{x}}$ into a unit-by-unit configuration, according to $\mathbf{x} = \mathsf{G}\tilde{\mathbf{x}}$. Applied to (38), we arrive at

$$\mathbf{x}^k = \mathsf{G}\tilde{\mathbf{x}}^k, \quad \mathsf{M} = \mathsf{G}\tilde{\mathsf{M}}\mathsf{G}^T, \quad \mathsf{C} = \mathsf{G}\tilde{\mathsf{C}}\mathsf{G}^T, \quad \mathsf{K} = \mathsf{G}\tilde{\mathsf{K}}\mathsf{G}^T \tag{40}$$

and the temporal advancement over one time step (now in block-circulant form) reads

$$\mathsf{M}\mathbf{x}^{k+1} + \mathsf{C}\mathbf{x}^k + \mathsf{K}\mathbf{x}^{k-1} = 0. \tag{41}$$

Following Sec. II, we assess the long-time stability of the linearized dynamics by computing modal solutions of the global matrix. Introducing $\mathbf{x} = \hat{\mathbf{x}}e^{\lambda t}$ into Eq. (41), we arrive at the quadratic eigenvalue problem

$$(\sigma^2 \mathsf{M} + \sigma \mathsf{C} + \mathsf{K})\hat{\mathbf{x}} = 0, \quad \sigma = e^{\lambda \Delta t}. \tag{42}$$
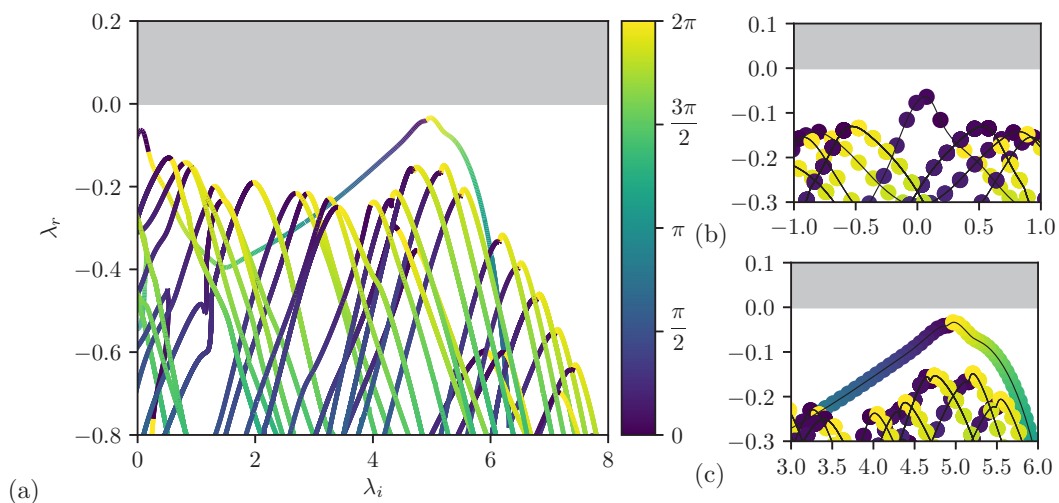
(a)

(b)

(c)

FIG. 10. Continuously parametrized spectrum describing the dynamics of perturbations for a linear cascade; the vertical axis represents the temporal growth rate λ_r and the horizontal axis indicates the angular frequency λ_i. (a) The line spectra are colored by the angle $\theta \in [0, 2\pi]$, parametrizing the unit circle $z = \exp(i\theta)$ in Eq. (28). (b) and (c) Zoom in on the least-damped regions and discretization of the continuously parametrized symbol curves by selecting $n = 54$ blade passages (depicted in closed circles).

As stated before, the matrices M, C, and K are block circulant; therefore we introduce the nth roots of unity ρ_j and express the eigenvector of the full system $\hat{\mathbf{x}}$ as

$$\hat{\mathbf{x}} = \begin{pmatrix} \hat{\mathbf{x}}_j \\ \rho_j \hat{\mathbf{x}}_j \\ \vdots \\ \rho_j^{n-2} \hat{\mathbf{x}}_j \\ \rho_j^{n-1} \hat{\mathbf{x}}_j \end{pmatrix}, \tag{43}$$

where $\hat{\mathbf{x}}_j$ satisfies a quadratic eigenvalue problem for a modified unit given by

$$(\sigma^2 \hat{\mathsf{M}}_j + \sigma \hat{\mathsf{C}}_j + \hat{\mathsf{K}}_j)\hat{\mathbf{x}}_j = 0, \quad j = 0, \dots, n-1 \tag{44}$$

and

$$\hat{\mathsf{M}}_j = \mathsf{M}_0 + \rho_j \mathsf{M}_1 + \mathsf{M}_2/\rho_j, \tag{45a}$$

$$\hat{\mathsf{C}}_j = \mathsf{C}_0 + \rho_j \mathsf{C}_1 + \mathsf{C}_2/\rho_j, \tag{45b}$$

$$\hat{\mathsf{K}}_j = \mathsf{K}_0 + \rho_j \mathsf{K}_1 + \mathsf{K}_2/\rho_j, \tag{45c}$$

with $\mathsf{M}_{0,1,2}$, $\mathsf{C}_{0,1,2}$, and $\mathsf{K}_{0,1,2}$ extracted from the 3-periodic system (40).

The above eigenvalue problems have been solved using the software package SLEPc [45] together with the sparse direct solver MUMPS [46] and the shift-invert technique. The spectrum of the operator has been computed for different shift values and is shown in Figs. 10(a)–10(c). More specifically, we display the continuously parametrized symbol curves, as defined by Eq. (28). These curves describe the spectrum in the limit of an infinite system, without any *a priori* decision on a specific number of individual units. The computations are performed on a three-blade passage system. Figure 10(a) clearly displays line spectra, parametrized by an angle $\theta \in [0, 2\pi]$, which represent the mapping of the unit circle $z = \exp(i\theta)$ under the nearest-neighbor coupled system. The largest modal growth is

achieved for frequencies of $\lambda_i \sim 4.8$, but a preference of very-low-frequency modes ($\lambda_i \sim 0.1$) is also expected due to a weak damping of these structures. Figures 10(b) and 10(c) highlight these important parts of the spectrum and show a "discretization" of these continuously parametrized spectral lines, given by selecting $n = 54$ units. Based on the line spectra, we can assess the sensitivity of the system to the number of individual units, estimate the number of units for weakest modal damping (or largest modal amplification), and predict the Bloch wavelength (root of unity) of this least-damped, most-amplified structure.

As an example of a nonmodal analysis in n-periodic fluid systems we consider the input-output analysis described in Sec. II C. First, we introduce a harmonic forcing in the momentum equation $\mathbf{f} = \hat{\mathbf{f}} e^{i\omega t}$; the asymptotic response $\mathbf{x} = \hat{\mathbf{x}} e^{i\omega t}$ is then given by $\hat{\mathbf{x}} = \mathsf{R}(\omega)\mathsf{B}\hat{\mathbf{f}}$, with

$$\mathsf{R}(\omega) = (\mathsf{M}e^{i\omega\Delta t} + \mathsf{C} + \mathsf{K}e^{-i\omega\Delta t})^{-1} \, \frac{e^{i\omega\Delta t} - 1}{i\omega} \, . \tag{46}$$

The matrix $\mathsf{R}(\omega)$ is the resolvent operator and the matrix B is defined such that the forcing terms are only introduced in the momentum equation. For a given angular frequency ω we then maximize the gain by optimizing over all harmonic forcings $\hat{\mathbf{f}}$; this optimal gain can be expressed in terms of the singular-value decomposition of $\mathsf{R}(\omega)\mathsf{B}$ according to

$$G^*(\omega) = \max_{\hat{\mathbf{f}}} \frac{\|\mathsf{R}(\omega)\mathsf{B}\hat{\mathbf{f}}\|}{\|\hat{\mathbf{f}}\|} = \|\mathsf{R}(\omega)\mathsf{B}\| = \sigma_1[\mathsf{R}(\omega)\mathsf{B}], \tag{47}$$

with σ_1 denoting the leading singular value. As before, the computational cost associated with the above calculation can be simplified by exploiting the block-circulant structure of the resolvent operator. We thus compute optimal gain G^* as

$$G^*(\omega) = \max_{j} \|\hat{\mathsf{R}}_j(\omega)\hat{\mathsf{B}}_0\|, \tag{48}$$

where

$$\hat{\mathsf{R}}_j(\omega) = (\hat{\mathsf{M}}_j e^{i\omega\Delta t} + \hat{\mathsf{C}}_j + \hat{\mathsf{K}}_j e^{-i\omega\Delta t})^{-1} \frac{e^{i\omega\Delta t} - 1}{i\omega}, \quad \hat{\mathsf{B}}_0 = \begin{pmatrix} \mathsf{I} \\ \mathsf{0} \end{pmatrix}. \tag{49}$$
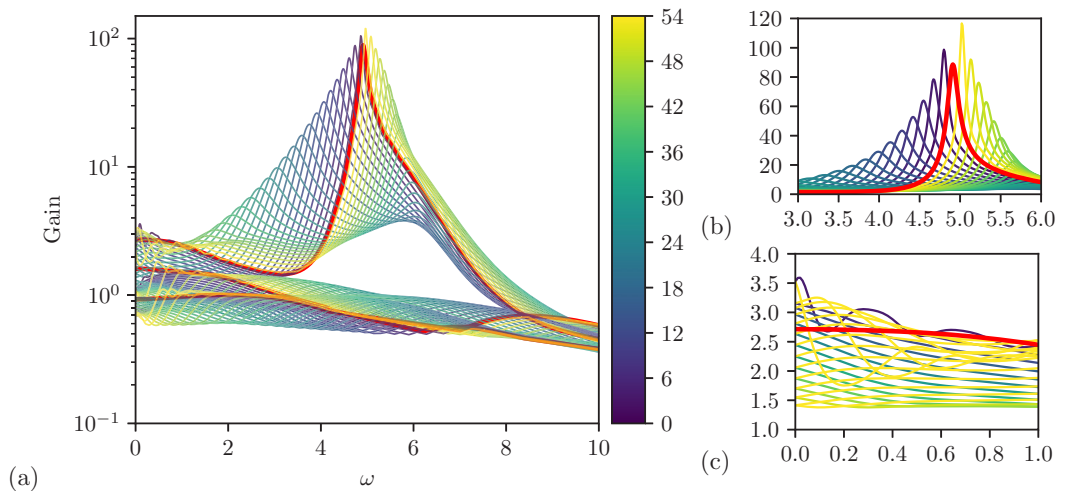

FIG. 11. Optimal gains for varying angular frequency. The curves have been colored according to their corresponding root of unity. The optimal gain for $j = 0$ is displayed in red. A closer view is presented in the range of (b) amplified wake instabilities and (c) low-frequency dynamics.

In Fig. 11 we present the singular values of the operator $\hat{\mathsf{R}}_j(\omega)\hat{\mathsf{B}}_0$ as a function of the angular frequency ω. The singular values for the fully periodic case, i.e., $j = 0$, are indicated in red, whereas the remaining curves are colored according to their corresponding root of unity: The case $j = 1$ is shown in dark blue and the case $j = 53$ in yellow; starting from these two cases, the color scheme for higher and lower values of j gradually tends to green. It is apparent from the figure that the maximum amplification at most frequencies is reached for cases that are not purely periodic; only at rather narrow frequency windows ($\omega \approx 9.5$, $\omega \approx 4.9$, $\omega \approx 0.85$, and $\omega \approx 0.55$) does the response
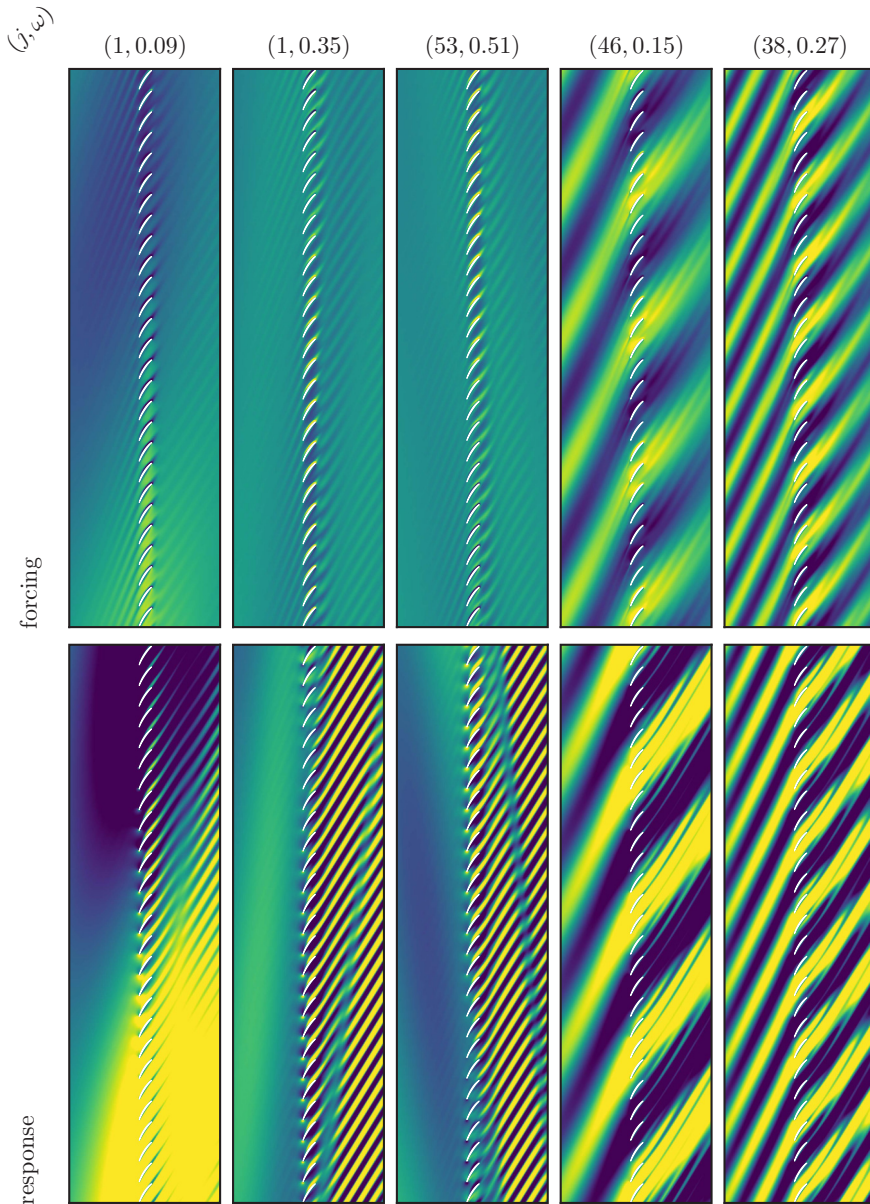

FIG. 12. Optimal forcing and response flow fields from a nonmodal resolvent analysis of a 54-periodic linear blade cascade for selected (low) frequencies. The periodicity j, at which the maximal gain has been obtained, is indicated on top of the subplots, together with the chosen forcing frequency.

behavior with single-subunit periodicity (i.e., with $j = 0$) constitute the optimal gain to harmonic forcing.

Exploring the lower frequencies more closely, we recover the optimal forcing $\hat{\mathbf{f}}$ and resulting optimal response $\hat{\mathbf{x}}$ in the 54-blade linear cascade for a given frequency. This is accomplished using the singular-value decomposition of the subunit matrices $\hat{\mathsf{R}}_j(\omega)\hat{\mathsf{B}}_j$: The principal singular vectors, evaluated for the value of j that constitutes the maximal gain $G^*(\omega)$, represent the spatial fields of
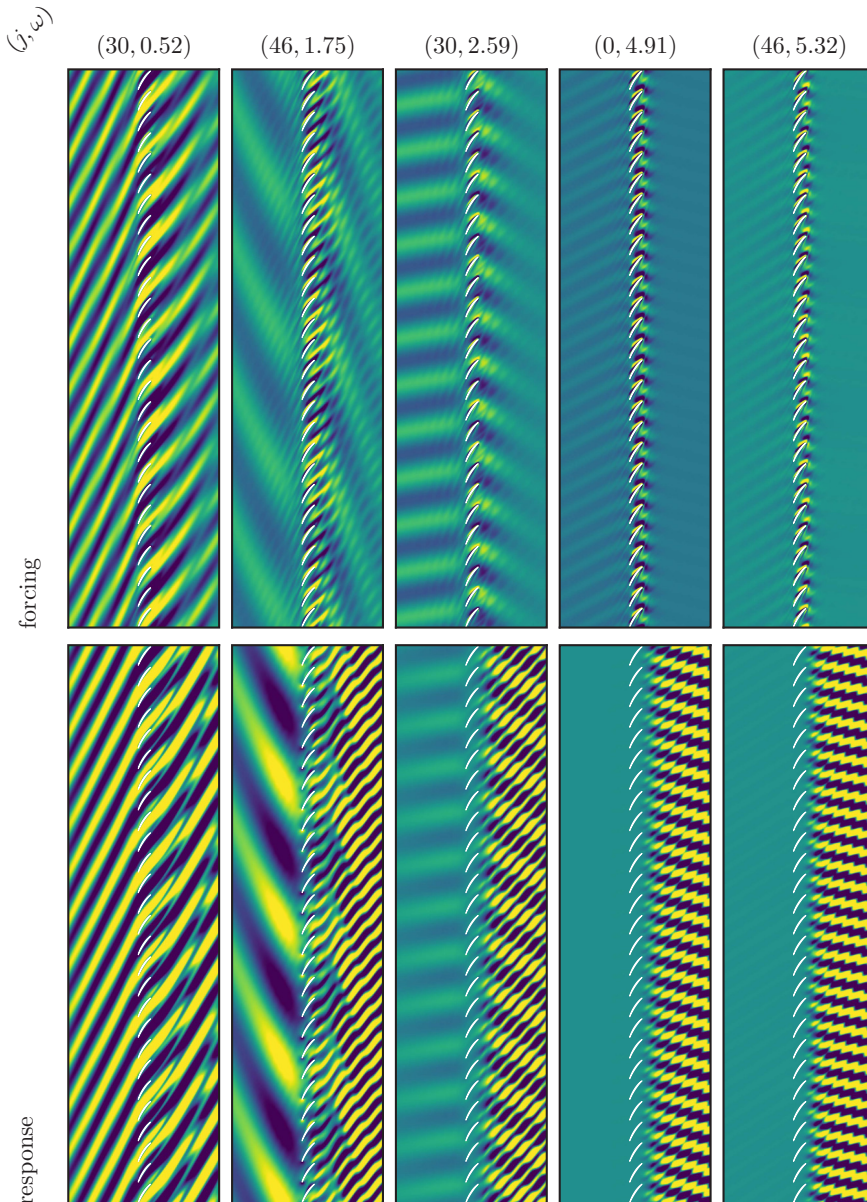

FIG. 13. Optimal forcing and response flow fields from a nonmodal resolvent analysis of a 54-periodic linear blade cascade for selected (higher) frequencies. The periodicity j, at which the maximal gain has been obtained, is indicated on top of the subplots, together with the chosen forcing frequency.

the optimal harmonic input and output structures, once they have been restored to the global domain using (18). For selected low frequencies they are displayed in Fig. 12.

As the maximal gain for a given frequency is achieved for different values of j, the associated spatial structures reflect the respective periodicity along the linear 54-blade cascade. For a very low forcing frequency of $\omega = 0.09$ the ($j = 1$) subproblem constitutes the maximum response of the 54-periodic system and both the forcing and the response are characterized by a modulation along the transverse direction that links and synchronizes the motion across many blades. This modulation, on top of a blade-geometry-induced periodicity, is clearly visible in Fig. 12 for $(j,\omega) = (1,0.09)$, $(1,0.35)$, and $(53,0.51)$, in particular in the response fields. This multiperiodic trend is continued for higher frequencies, as shown in Fig. 12 for $(j,\omega) = (46,0.15)$ and $(38,0.27)$, where synchronized groups of four and two blades, respectively, dominate the optimal forcing and response flow fields. In this case, the 1-periodic structures induced by the blade geometry are far less discernible. From this analysis, it can be concluded that forcing at low frequencies favors and induces large-scale motion that yields a locked dynamics across multiple blade passages, resulting in traveling structures with transverse wavelengths that exceed the periodicity imposed by the blade geometry.

As we progress to higher forcing frequencies, the appearance of periodicity other than the one associated with $j = 0$ is still noticeable, although to a lesser extent. Figure 13 depicts a selection of optimal forcing and response structures for frequencies above $\omega \approx 0.5$. For the frequencies $\omega = 0.52$, 1.75, and 2.59 (with associated optimal root-of-unity values of $j = 30$, 46, and again 30) we observe a clear lower-frequency modulation imposed on the periodic structures forced by the blade geometry. For a forcing frequency of $\omega = 4.91$ we obtain a fully periodic ($j = 0$) structure; however, the range of frequencies where this structure is dominant is rather narrow, as can be seen in Fig. 11. For slightly larger (or smaller) frequencies, periodicities other than the $j = 0$ case are favored, even though their contribution to the forcing and response flow field is smaller [see the rightmost panel in Fig. 13 for $(j,\omega) = (46,5.32)$].

IV. CONCLUSION

A computational framework for the analysis of fluid systems that consist of n identical units with nearest-neighbor or global coupling has been presented and demonstrated on a range of problems. This framework is based on the fact that the block-circulant nature of the global system matrices yields simplified expressions and associated algorithms that only contain matrices that describe the dynamics of a single unit and its coupling to other (identical) units. The analysis of n-periodic fluid systems can thus be formulated and performed efficiently at the cost of single-unit computations and executed in parallel, while still capturing the global dynamics and fluid structures that span multiple subunits.

While the framework is closely linked to Floquet theory, Bloch wave methodology, and related techniques for modified boundary conditions, it provides simple and efficient techniques that require minimally invasive modifications of computer codes to enable the type of investigations presented in this study. Compact expressions for the analysis of modal and nonmodal flow characteristics, for the response to impulses or to harmonic forcing, for the quantification of input-output behavior and cross-unit dynamics, and for direct-adjoint techniques have been given. They furnish tools for the investigation of fluid systems that contain periodicity in the form of geometric features or as an assembly of identical units.

The framework has been showcased on various problems of increasing complexity, from a simple model problem describing flow along a grooved wall to interacting arrays of wakes (as for example encountered in heat exchangers) to the incompressible flow through a linear blade cascade. The full set of tools has been applied and a common feature of the analyses has been the presence, and often dominance, of large-scale motion that spans more than one subunit and would be missed by an analysis that imposes periodic boundary conditions over one subunit. For example, the flow over a spanwise array of roughness elements is often modeled by a fundamental computational box that contains one roughness element and enforces periodic boundary conditions in the spanwise direction.

Similarly, instabilities that show a preference for a specific spanwise scale are commonly studied by concentrating on a fundamental wavelength in the spanwise direction together with periodic boundary conditions. The examples in this article clearly demonstrate that, in both cases, geometries that consist of multiple copies of this fundamental computational box could support motion and instabilities that span several subunits, but that are not captured by a fully periodic assumption across one subunit.

It is hoped that the computational techniques presented in this article will help in the proper analysis of n-periodic fluid systems arising in a wide range of applications from science and engineering.

---

[1] F. M. Esquivelzeta-Rabell, B. Figueroa-Espinoza, D. Legendre, and P. Salles, Shearing flow over an idealized wavy surface: Comparison between linear theory and DNS, Proceedings of the Third Brazilian Conference on Boiling, Condensation and Multiphase Flow, Curitiba, 2012 (unpublished).

[2] N. K. Ghaddar, K. Z. Korczak, B. B. Mikic, and A. T. Patera, Numerical investigation of incompressible flow in grooved channels. Part 1. Stability and self-sustained oscillations, J. Fluid Mech. **163**, 99 (1986).

[3] N. K. Ghaddar, M. Magen, B. B. Mikic, and A. T. Patera, Numerical investigation of incompressible flow in grooved channels. Part 2. Resonance and oscillatory heat-transfer enhancement, J. Fluid Mech. **168**, 541 (1986).

[4] J. Szumbarski, Instability of viscous incompressible flow in a channel with transversely corrugated walls, J. Theor. Appl. Mech. **45**, 659 (2007).

[5] M. Choudhari, F. Li, and J. Edwards, Stability analysis of roughness array wake in a high-speed boundary layer, *Proceedings of the 47th AIAA Aerospace Sciences Meeting including The New Horizons Forum and Aerospace Exposition* (AIAA, Reston, 2009), paper 2009-0170.

[6] S. D. M. Adams, R. V. Craster, and S. Guenneau, Bloch waves in periodic multi-layered acoustic waveguides, Proc. R. Soc. A **464**, 2669 (2008).

[7] X. Garnaud and C. C. Mei, Bragg scattering and wave-power extraction by an array of small buoys, Proc. R. Soc. A **466**, 79 (2010).

[8] J. I. Erdos, E. Alznert, and W. McNally, Numerical solution periodic transonic flow through a fan stage, AIAA J. **15**, 1559 (1977).

[9] G. A. Gerolymos and V. C. Chapin, Generalized expression of chorochronic periodicity in turbomachinery blade-row interaction, Rech. Aérospat. **5**, 69 (1991).

[10] G. A. Gerolymos, G. J. Michon, and J. Neubauer, Analysis and application of chorochronic periodicity in turbomachinery rotor/stator interaction computations, J. Propul. Power **18**, 1139 (2002).

[11] L. He, Fourier methods for turbomachinery applications, Prog. Aero. Sci. **46**, 329 (2010).

[12] H. D. Li and L. He, Single-passage solution of three-dimensional unsteady flows in a transonic fan rotor, Proc. Inst. Mech. Eng. A **215**, 653 (2001).

[13] H. D. Li and L. He, Single-passage analysis of unsteady flows around vibrating blades of a transonic fan under inlet distortion, ASME J. Turbomach. **124**, 285 (2002).

[14] M. Olaussona, L.-E. Eriksson, and S. Baralon, Evaluation of nonlinear rotor wake/stator interaction by using time domain chorochronic solver, Proceedings of the 8th International Symposium on Experimental

and Computational Aerothermodynamics of Internal Flows, Lyon, 2007 (unpublished), paper ISAIF8-0064.

[15] G. Campa and S. M. Camporeale, Prediction of the thermoacoustic combustion instabilities in practical annular combustors, J. Eng. Gas Turbines Power **136**, 091504 (2014).

[16] G. A. Mensah, G. Campa, and J. P. Moeck, Efficient computation of thermoacoustic modes in industrial annular combustion chambers based on Bloch-wave theory, J. Eng. Gas Turbines Power **138**, 081502 (2016).

[17] J. P. Moeck, M. Paul, and C. O. Paschereit, Thermoacoustic instabilities in an annular Rijke tube, *ASME Turbo Expo 2010: Power for Land, Sea, and Air* (ASME, New York, 2010), paper GT2010-23577.

[18] S. Patil, T. Sedalor, D. Tafti, S. Ekkad, Y. Kim, P. Dutta, H.-K. Moon, and R. Srinivasan, Study of flow and convective heat transfer in a simulated scaled up low emission annular combustor, J. Thermal Sci. Eng. Appl. **3**, 031010 (2011).

[19] G. Staffelbach, L. Y. M. Gicquel, G. Boudier, and T. Poinsot, Large eddy simulation of self excited azimuthal modes in annular combustors, Proc. Comb. Inst. **32**, 2909 (2009).

[20] S. R. Stow and A. P. Dowling, Modelling of circumferential modal coupling due to Helmholtz resonators, *ASME Turbo Expo 2003, collocated with the 2003 International Joint Power Generation Conference* (ASME, New York, 2003), paper GT2003-38168.

[21] P. Wolf, G. Staffelbach, A. Roux, L. Y. M. Gicquel, T. Poinsot, and V. Moureau, Massively parallel LES of azimuthal thermo-acoustic instabilities in annular gas turbines, C. R. Mec. **337**, 385 (2009).

[22] K. Ekici and K. C. Hall, Nonlinear analysis of unsteady flows in multistage turbomachines using the harmonic balance technique, *Proceedings of the 44th AIAA Aerospace Sciences Meeting and Exhibit* (AIAA, Reston, 2006), paper 2006-0422.

[23] A. K. Gopinath, E. van der Weide, J. J. Alonso, and A. Jameson, Three-dimensional unsteady multi-stage turbomachinery simulations using the harmonic balance technique, *Proceedings of the 45th AIAA Aerospace Sciences Meeting and Exhibit* (AIAA, Reston, 2007), paper 2007-0892.

[24] F. Bloch, Über die Quantenmechanik der Elektronen in Kristallgittern, Z. Phys. **52**, 555 (1929).

[25] L. N. Trefethen and M. Embree, *Spectra and Pseudospectra: The Behavior of Non-Normal Matrices and Operators* (Princeton University Press, Princeton, 2005).

[26] R. M. Gray, Toeplitz and circulant matrices: A review, Found. Trends Commun. Inf. Theory **2**, 155 (2006).

[27] D. S. G. Pollock, Circulant matrices and time-series analysis, Int. J. Math. Edu. Sci. Technol. **33**, 213 (2010).

[28] G. J. Tee, Eigenvectors of block circulant and alternating circulant matrices, Res. Lett. Inf. Math. Sci. **8**, 123 (2005).

[29] P. J. Schmid, Nonmodal stability theory, Annu. Rev. Fluid Mech. **39**, 129 (2007).

[30] P. J. Schmid and D. S. Henningson, *Stability and Transition in Shear Flows* (Springer, New York, 2001).

[31] M. R. Jovanovic and B. Bamieh, Componentwise energy amplification in channel flows, J. Fluid Mech. **534**, 145 (2005).

[32] P. Luchini and A. Bottaro, Adjoint equations in stability theory, Annu. Rev. Fluid Mech. **46**, 493 (2014).

[33] V. Mehrmann and H. Voss, Nonlinear eigenvalue problems: A challenge for modern eigenvalue methods, GAMM Mitteil. **27**, 121 (2004).

[34] F. Tisseur and K. Meerbergen, The quadratic eigenvalue problem, SIAM Rev. **43**, 235 (2001).

[35] J. Martins, P. Sturdza, and J. Alonso, The complex-step derivative approximation, ACM Trans. Math. Softw. **29**, 245 (2003).

[36] J. Peter and R. P. Dwight, Numerical sensitivity analysis for aerodynamic optimization: A survey of approaches, Comput. Fluids **39**, 373 (2010).

[37] L. Hascoët and V. Pascual, The Tapenade automatic differentiation tool: Principles, model, and specification, ACM Trans. Math. Softw. **39**, 20 (2013).

[38] M. Fosas de Pando, D. Sipp, and P. J. Schmid, Efficient evaluation of the direct and adjoint linearized dynamics from compressible flow solvers, J. Comput. Phys. **231**, 7739 (2012).

[39] The latest version of the code will be available in doi: 10.5281/zenodo.1040159.

[40] K. Taira and T. Colonius, The immersed boundary method: A projection approach, J. Comput. Phys. **225**, 2118 (2007).

[41] C. S. Peskin, The immersed boundary method, Acta Numer. **11**, 1 (2002).

[42] A. M. Roma, C. S. Peskin, and M. J. Berger, An adaptive version of the immersed boundary method, J. Comput. Phys. **153**, 509 (1999).

[43] C. L. Ball, Advanced technology impact on compressor design and development: A perspective, NASA Report No. TM-102341, 1989 (unpublished).

[44] W. B. Gardner, Energy efficient engine (E3) technology status, *Proceedings of the 20th Aerospace Sciences Meeting* (AIAA, Reston, 1982), paper 1982-1052.

[45] V. Hernandez, J. E. Roman, and V. Vidal, SLEPc: A scalable and flexible toolkit for the solution of eigenvalue problems, ACM Trans. Math. Softw. **31**, 351 (2005).

[46] P. R. Amestoy, I. S. Duff, and J.-Y. L'Excellent, Multifrontal parallel distributed symmetric and unsymmetric solvers, Comput. Methods Appl. Mech. Eng. **184**, 501 (2000).